Heat Transfer and Fluid Flow during Gas-Metal-Arc Fillet Welding for Various Joint Configurations and Welding Positions

A. KUMAR and T. DEBROY

Gas-metal-arc (GMA) fillet welding is one of the most commonly used welding processes in the industry. This welding process is characterized by the complex joint geometry, a deformable weld pool surface, and the addition of hot metal droplets. In this work, a three-dimensional numerical heat-transfer and fluid-flow model is developed to capture the effects of the tilt angle of the fillet joint and the welding positions, *i.e.*, V, L, and other configurations on the temperature profiles, velocity fields, weld pool shape, weld pool free surface profile, thermal cycles, and cooling rates during GMA welding in spray mode. The governing equations of conservation of mass, momentum, and energy are solved using a boundary fitted curvilinear coordinate system. The weld pool free surface deformation is calculated by minimizing the total surface energy. A dimensional analysis is performed to understand the importance of heat transfer by conduction and convection and the role of various driving forces on convection in the liquid weld pool. The computed shape and size of the fusion zone, finger penetration characteristic of the GMA welds, and the solidified free surface profile are in fair agreement with the corresponding experimental results. The calculated cooling rates are also in good agreement with independent experimental data. The results reported here indicate a significant promise for understanding the effect of joint orientations and welding positions on weld pool shape, size, and the cooling rates based on fundamental principles of transport phenomena.

DOI: 10.1007/s11661-006-9083-4

I. INTRODUCTION

PREVIOUS computer modeling efforts to simulate and understand various welding processes through transport phenomena-based models have focused either on simple butt joints of rectangular workpiece or the symmetrical V-shaped fillet joints.[1,2,3] However, the fillet joint is not symmetrical in many practical situations. Depending on the structure, the welding is generally performed either by tilting the fillet joint or by lifting the workpiece. The inclinations of the workpiece and welding positions (*i.e.* downhill, flat, and uphill) affect the weld pool convective flow and hence the weld bead profile, thermal cycles, and cooling rates inside the workpiece. Furthermore, most of the previous models did not consider the effect of arc pressure on weld pool surface deformation.[4–11] Depending on the current and the voltage levels, the arc can exert significant pressure on the surface of the weld pool that deforms the free surface.[1–3,12–15] The deformation of the weld pool surface affects the heat transfer, fluid flow, and solidified weld bead geometry.[1,2,13–17] The purpose of this study is to investigate how the temperature distribution, velocity fields, free surface profile, and cooling rates change with uphill or downhill welding positions and workpiece orientation, *i.e.*, V, L, and other configurations during GMA fillet welding. Such modeling of the GMA fillet welding process is important because an improved understanding of the underlying physics would lead to better welds.

In this article, a numerical model is developed to consider the orientations of fillet joint; welding positions such as downhill, flat, and uphill welding; and the deformation of the weld pool free surface during GMA welding in spray mode. The weld pool surface profile is calculated by minimizing the total surface energy, which includes the surface tension energy, gravity potential, and work done by arc force. The impingement of droplets on the weld pool surface is considered *via* a volumetric heat source. This model is used to investigate the heat transfer and fluid flow during GMA fillet welding of A-36 mild steel. The calculated weld bead shape is compared with the corresponding experimental result. A dimensional analysis is performed to understand the role of various driving forces on convection in the liquid weld pool. The effects of various welding parameters, welding positions, and workpiece orientations on weld bead geometry and cooling rates are quantitatively studied using the numerical model.

II. MATHEMATICAL FORMULATION

A. *Assumptions and Salient Features*

Because of the complexity of the GMA fillet welding, the following simplifying assumptions are made to make

A. KUMAR, Graduate student and T. DEBROY, Professor, are with the Department of Materials Science and Engineering, The Pennsylvania State University, University Park, PA 16802, USA. A. KUMAR is currently working as Senior Research Engineer at ExxonMobil Upstream Research Company, Houston, TX, USA. Contact e-mail: axk927@gmail.com

Manuscript submitted June 22, 2006.
Article published online April 13, 2007.

the computational work tractable.[1,2,3] (a) The thermophysical properties such as thermal diffusivity and the specific heat needed for the calculations are taken at 1745 °C because the values of these variables were not readily available for the temperature range of interest. (b) The additional heat transported by the droplets into the weld pool is taken into account by using a time-averaged volumetric heat source, which has been widely used in the literature.[12,19] (c) The heat flux from the arc is assumed to have a Gaussian distribution on the top surface.[1–11]

B. *Governing Equations*

The welding problem is assumed to be at steady state by using a coordinate system attached to the heat source. Therefore, the heat transfer and fluid flow during welding can be calculated by solving the following governing equations:[1–4,7]

$$\frac{\partial u_i}{\partial x_i} = 0 \qquad [1]$$

$$\rho \frac{\partial (u_i u_j)}{\partial x_i} = \frac{\partial}{\partial x_i}\left(\mu \frac{\partial u_j}{\partial x_i}\right) + S_j \qquad [2]$$

$$\rho \frac{\partial (u_i h)}{\partial x_i} = \frac{\partial}{\partial x_i}\left(\alpha \frac{\partial h}{\partial x_i}\right) - \rho L \frac{\partial (u_i f_l)}{\partial x_i} - \rho U_w \frac{\partial h}{\partial x_1} - \rho U_w L \frac{\partial f_l}{\partial x_1} + S_v \qquad [3]$$

Equations [1], [2], and [3] are the continuity, momentum conservation, and energy conservation equations, respectively. In these equations, subscripts i and j indicate the coordinate direction ($i, j = 1$, 2, and 3), x is the distance, u is the liquid metal velocity, ρ is the density, μ is the viscosity, S_j is the source term for the jth momentum equation, h is the sensible heat, α is the thermal diffusion coefficient (defined as $\alpha = k/C_p$, where k is the thermal conductivity and C_p is the specific heat), U_w is the material moving speed (parallel to the positive x direction, *i.e.*, $i = 1$ direction), L is the latent heat of fusion, and S_v is a source term accounting for the additional heat from metal droplets. The source term S_j used in Eq. [2] can be written as[1–4,7,23,24]

$$S_j = -\frac{\partial p}{\partial x_j} - \rho U_w \frac{\partial u_j}{\partial x_1} - C\left(\frac{(1-f_l)^2}{f_l^3 + B}\right) u_j + F_j^e + F_j^b + F_j^i \qquad [4]$$

where p represents pressure; f_l is the liquid metal fraction; and F_j^e, F_j^b, and F_j^i correspond to the electromagnetic, buoyancy, and inertia forces in the jth direction, respectively. In Eq. [4], the third term represents the frictional dissipation in the mushy zone according to the Carman–Kozeny approximation,[23,24] where B and C are two constants. The liquid metal fraction, f_l, is assumed to vary linearly with temperature inside the mushy zone:[1–4,7]

$$f_l = \begin{cases} 1 & T \geq T_l \\ \frac{T - T_s}{T_l - T_s} & T_s < T < T_l \\ 0 & T \leq T_s \end{cases} \qquad [5]$$

where T_l and T_s are the liquidus and solidus temperature of the material, respectively. The electromagnetic force, $\mathbf{F}^e$, is given as[25,26]

$$\mathbf{F}^e = \mathbf{J} \times \mathbf{B} \qquad [6]$$

where $\mathbf{J}$ and $\mathbf{B}$ are the current flux and magnetic field in the workpiece, respectively. Using the Boussinesq approximation, the gravity (buoyancy) force, $\mathbf{F}^b$, is given as[1–3,7]

$$\mathbf{F}^b = -\rho g \cos\left(\frac{\pi}{4} - \theta\right) \cos\varphi \beta (T - T_{\text{ref}}) \qquad [7]$$

where g is the acceleration due to gravity and is in the negative z direction; θ is the tilt angle or inclination of plates from the horizontal position; φ is the angle of lift from the horizontal plane, as shown in Figure 1; β is the thermal expansion coefficient; and T and T_{ref} are the local and arbitrarily selected reference temperatures. The inertia force, $\mathbf{F}^i$, is given as

$$\mathbf{F}^i = -\rho g \sin\varphi \mathbf{i} + \rho g \cos\left(\frac{\pi}{4} - \theta\right)\mathbf{j} \qquad [8]$$

where i and j are the unit vectors in the x and y directions, respectively.

The heat flux from the arc is assumed to be a Gaussian distribution at the weld top surface. For the bottom surface, the heat flux, F_b, is given as[1,3]

$$\alpha \nabla h \cdot \mathbf{n}_b = F_b = h_c (T - T_a) \qquad [9]$$

where $\mathbf{n}_b$ is a unit normal vector to the bottom surface, h_c is the convective heat-transfer coefficient, and T_a is the ambient temperature (a value of 298 K is used). The temperatures at other surfaces, *i.e.*, east, west, south, and north surfaces, are set to the ambient temperature.

An important feature of the GMA welding is the finger penetration, which is mainly caused by the transfer of heat from the superheated metal droplets into the weld pool. In the present work, the droplet heat transfer is effectively simulated by incorporating a time-averaged volumetric heat source term (S_v) in the energy conservation equation. More details about the calculation of the volumetric heat source based on the available knowledge base of the interaction between metal droplets and the weld pool for various welding conditions are available in the literature.[1,3,18,19,27,28]

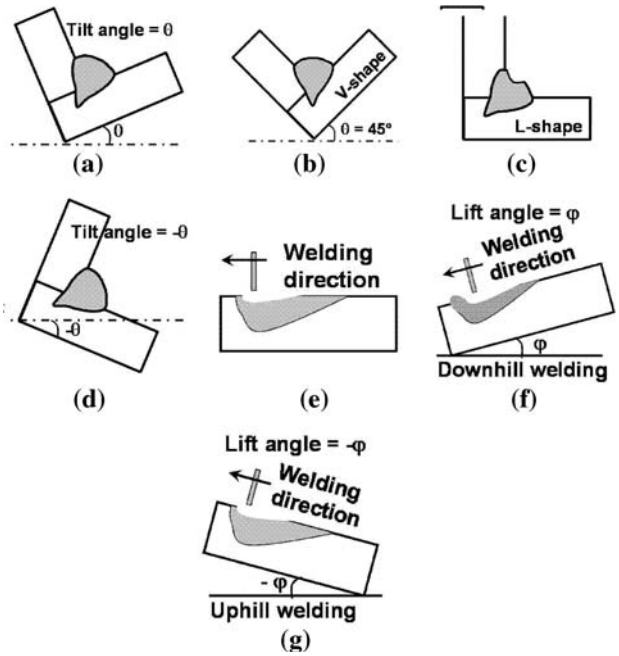

Fig. 1—Schematic illustration of fillet joint in various orientations. (a) through (d) show the transverse section of the fillet joint perpendicular to the welding direction, while (e) through (g) show the central longitudinal section of the fillet joint parallel to the welding direction. (*a*) Fillet joint with tilt angle θ, (*b*) symmetric V-shaped joint, (*c*) L-shaped joint, (*d*) fillet joint with tilt angle $-\theta$, (*e*) welding in flat position, (*f*) downhill welding with lift angle = φ, and (*g*) uphill welding with lift angle = $-\varphi$.

C. *Calculation of the Weld Pool Top Surface Profile*

During GMA fillet welding, the weld pool top surface under the electrode is depressed by the arc force. Therefore, the pool top surface is not flat and the surface profile needs to be determined. At steady state, the weld pool surface can be determined by using the energy minimization method. The total energy to be minimized includes the surface energy due to the change in area of the weld surface, the potential energy in the gravitational field, and the work performed by the arc pressure displacing the weld pool surface, as shown subsequently:

(Total energy) = (the surface energy) + (the gravitational potential energy) – (the work performed by the arc pressure)

The z-axis and the surface profile, ϕ, are defined as the opposite direction of gravity and arc pressure. The surface energy, E_s, evaluated in the small area A_s is then given as[18,21]

$$E_s = \sigma \iint_s \left[1 + \left(\frac{\partial \phi}{\partial x}\right)^2 + \left(\frac{\partial \phi}{\partial y}\right)^2\right]^{1/2} dxdy \qquad [10]$$

where σ is the surface tension of the molten metal. The potential energy, E_g, increases by the deformation of surface and can be written in the following form:

$$E_g = \iiint \rho g\left[\phi \cos\left(\frac{\pi}{4} - \theta\right) - y \sin\left(\frac{\pi}{4} - \theta\right) - x \sin\varphi\right] dxdydz$$
$$= \iint \rho g\left[\frac{\phi^2}{2}\cos\left(\frac{\pi}{4} - \theta\right) - \phi y \sin\left(\frac{\pi}{4} - \theta\right) - \phi x \sin\varphi\right] dxdy \qquad [11]$$

where θ is the titling of the workpiece from the horizontal position and φ is the angle of lift from the horizontal plane, as shown in Figure 1. The surface tension, σ, is assumed to vary with temperature as follows:[29,30]

$$\sigma(T) = \sigma(T_l) + \left(\frac{d\sigma}{dT}\right)(T - T_l) \qquad [12]$$

where T_l is the liquidus temperature of metal.

The arc pressure energy, E_p, is equal to the work done by arc pressure (W_p) but with a negative sign. In the current coordinate system, the arc energy increases by the deformation as follows:[31,32]

$$E_p = -W_p = \iint P_a \phi dxdy \qquad [13]$$

where P_a is the arc pressure. The arc pressure is assumed as the following Gaussian distribution:[31,32]

$$P_a(r) = P_{\max} \exp\left(-\frac{3r^2}{r_a^2}\right) \qquad [14]$$

where r_a is a 95 pct effective radius of arc pressure (*i.e.*, $\mathrm{Pa}(r_a) = 0.95 \times P_{\max}$). In free surface modeling, an adjustment of the maximum arc pressure is accompanied with the change of the pressure distribution parameter to conserve total arc force, which can be calculated as follows:

$$F = \int 2\pi r P_a dr \qquad [15]$$

So, if the total arc force is conserved, the following equation is preferred rather than Eq. [14]:

$$P_a = \frac{F}{2\pi\sigma_P^2} \exp\left(-\frac{x^2 + y^2}{2\sigma_p^2}\right) \qquad [16]$$

The total arc force was calculated by numerical integration of experimental results by Lin and Eagar.[31] The pressure distribution parameters are also given by the Gaussian fitting. At a specific tip angle, the total arc force and the pressure distribution parameter are linearly modeled with respect to the welding current, I (A), as follows:[1,18]

$$F\,(\mathrm{N}) = \begin{cases} -0.06049 + 0.0002808 \times \mathrm{I} & (\text{for } 30\,\text{deg tip angle}) \\ -0.04017 + 0.0002553 \times \mathrm{I} & (\text{for } 60\,\text{deg tip angle}) \\ -0.04307 + 0.0001981 \times \mathrm{I} & (\text{for } 90\,\text{deg tip angle}) \end{cases} \quad [17]$$

$$\sigma_P(\mathrm{mm}) = \begin{cases} 0.7725 + 0.00193 \times \mathrm{I} & (\text{for } 30\,\text{deg tip angle}) \\ 1.4875 + 0.00123 \times \mathrm{I} & (\text{for } 60\,\text{deg tip angle}) \\ 1.4043 + 0.00174 \times \mathrm{I} & (\text{for } 90\,\text{deg tip angle}) \end{cases} \quad [18]$$

The total energy, E_t, was calculated by the following equation:

$$\begin{aligned} E_t &= E_s + E_s + E_p \\ &= \iint \left(\sigma\sqrt{1+\phi_x^2+\phi_y^2} + \rho g \left[\frac{\phi^2}{2}\cos\left(\frac{\pi}{4}-\theta\right) \right.\right. \\ &\quad \left.\left. -y\phi\sin\left(\frac{\pi}{4}-\theta\right) - x\phi\sin\varphi \right] + p_a\phi \right) dxdy \end{aligned} \quad (19)$$

The total energy is minimized by using the variational approach, with the constraint that the deposited area, A_{FW}, at a solidified cross section of the fillet weld is equal to the amount of fed wire per unit length. The constraining mass conservation equation is given by the following equation.[1,18]

$$\int (\phi_s - z_0)dy - \frac{\pi r_w^2 w_f}{U_w} = 0 \quad [20]$$

where ϕ_s is the solidified surface profile; z_0 is the z location of the workpiece top surface; and r_w, w_f, and U_W are the wire radius, wire feeding rate, and welding speed, respectively. From the Euler equation, the governing equation is derived as follows:

$$\begin{aligned} &\sigma\left\{ \frac{(1+\phi_y^2)\phi_{xx} - 2\phi_x\phi_y\phi_{xy} + (1+\phi_x^2)\phi_{yy}}{(1+\phi_x^2+\phi_y^2)^{3/2}} \right\} \\ &\quad = \rho g\left[\phi\cos\left(\frac{\pi}{4}-\theta\right) - y\sin\left(\frac{\pi}{4}-\theta\right) - x\sin\varphi \right] + P_a + \lambda \end{aligned} \quad [21]$$

where λ is the Lagrange multiplier. The governing Eq. [21] is solved using the Gauss–Seidel method.[33] After these calculations, the results are applied to the constraining Eq. [20], and the calculation is repeated after modification of the Lagrange multiplier, λ, to satisfy the constraining equation. The value of λ is obtained by using the bisection method.[33]

For fillet welding, the numerical solution of heat transfer and fluid flow with a deformable weld pool surface and complex joint geometry requires the use of a nonorthogonal deformable curvilinear grid system.[34,35] Therefore, the governing equations are transformed from the Cartesian to curvilinear coordinate system. The transformed governing equations were discretized using the control volume method, where the computational domain was divided into small rectangular control volumes. A scalar grid point was located at the center of each control volume, storing the values of scalar quantities such as pressure and enthalpy. Velocity components were stored at the control volume faces, staggered with respect to scalar locations. Discretized equations for a variable were formulated by integrating the corresponding governing equation over the control volumes in the computational domain. A power-law-based scheme was used to describe the convective flux at the control volume faces. A modified semi-implicit algorithm for pressure linked equations (SIMPLE) was used to solve the discretized equations.[36] The detailed information on the transformed equations in the curvilinear coordinate system and their discretization is available in the literature.[1,2,3]

Grid sensitivity tests were performed to select the optimal number of grids so that the results are not affected by their size and numbers. The solution domain had dimensions of 450 mm in length, 108 mm in width, and 18 mm in depth. Spatially, nonuniform grids with finer grids near the heat source were used for maximum resolution of variables. With the increase in number of grids, the accuracy of the calculation increases. However, with the increase in the number of grid points, the computation time increases. In the trade-off between accuracy and computation time, a $77 \times 66 \times 47$ grid system was selected for the calculation in this work because it provides the same solution as obtained with finer grid systems, and the calculations took about 20 minutes to converge in a PC with 3.2 GHz Intel P4 CPU and 2048 Mb PC2700 DDR-SDRAM memory (Hewlett-Packard, Palo Alto, CA).

III. RESULTS AND DISCUSSION

A. *Temperature Distribution, Velocity Field, and Free Surface Profile of Weld Bead*

The numerical heat-transfer and fluid-flow model was used for the calculation of temperature and velocity fields in the weld pool for different configurations of workpiece plates. The nominal composition of A-36 steel is maximum 0.29 pct C, 0.80 to 1.2 pct Mn, 0.04 pct P, 0.05 pct S, 0.15 to 0.3 pct Si, and remaining percentage Fe. The material properties for the A-36 steel workpiece[1,37] and the other data used in the calculations are presented in Table I. Figure 2 shows the temperature distribution, velocity fields, and free surface profile of the weld bead during GMA fillet welding of V-shaped symmetric joint in horizontal position. In this figure, the isotherms in front of the weld pool are compressed while those behind the weld pool are expanded because of the motion of the heat source. This figure also indicates that the depression of the grid lines is maximum under the arc, while the grids are elevated in the rear part of the weld pool. In these

Table I. Physical Properties of the A-36 Steel[1,37] and the Other Data Used in the Calculation

Name	Value
Liquidus temperature, T_l (K)	1785
Solidus temperature, T_s (K)	1745
Density of metal, ρ (kg m^{-3})	7.2×10^{3}
Thermal conductivity of solid, k_s (J m^{-1}·s^{-1}·K^{-1})	21.0
Specific heat of solid, C_{ps} (J kg^{-1}·K^{-1})	703.4
Specific heat of liquid, C_{pl} (J kg^{-1}·K^{-1})	808.1
Surface tension of liquid metal at melting point, γ (N m^{-1})	1.2
Temperature coefficient of surface tension, $d\gamma/dT$ (N m^{-1}·K^{-1})	-3.5×10^{-4}
Magnetic permeability, μ_m (N A^{-2})	1.26×10^{-6}
Coefficient of thermal expansion, β (K^{-1})	1.0×10^{-5}
Arc efficiency, η	54 pct
Arc radius, r_b (mm)	5.0
Convective heat-transfer coefficient, h_c (W mm^{-2} K^{-1})	42.0
Emissivity, ε	0.7
Ambient temperature, T_a (K)	298
Constant B in the Carman–Kozeny equation	1.0×10^{-7}
Constant C in the Carman–Kozeny equation	1.6×10^{4}

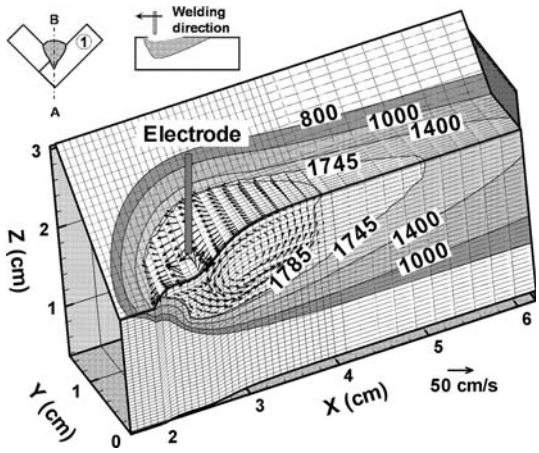

Fig. 2—Calculated temperature field and velocity fields during GMA welding of symmetrical V-shaped fillet joint in flat position. The temperatures are given in Kelvin. The thin solid lines represent the deformable grid system used in the calculation. For clarity, only a portion of the plate marked as 1 is shown in this figure.

figures, the weld pool boundary is represented by the 1745 K solidus isotherm of A-36 steel.

B. *Dimensionless Analysis to Calculate the Relative Importance of Various Driving Forces*

During GMA fillet welding, the energy from the arc is transported from the top surface of the weld pool to the surrounding solid region by both heat conduction and liquid metal convection. The heat-transfer rate inside the workpiece determines the peak temperature, shape of the weld pool, and temperature distribution in the heat-affected zone. Therefore, it is important to understand the effects of heat transfer by conduction and convection in the weld pool.

In the weld pool, heat is transported by a combination of convection and conduction. The Peclet number (Pe) can be used to determine the relative importance of convection *vs* conduction in transferring heat in the pool, which is given by following expression:

$$\mathrm{Pe} = \frac{\mathrm{heat}_{\mathrm{convection}}}{\mathrm{heat}_{\mathrm{conduction}}} = \frac{u_R \rho C_{pl} L_R}{k_l} \qquad [22]$$

where u_R and L_R are the characteristic velocity and length in the weld pool, respectively; ρ is the density; and C_{pl} and k_l are the specific heat and thermal conductivity of liquid metal, respectively. When the liquid metal convection significantly affects the heat transfer in the weld pool due to high liquid metal velocity and larger weld pool size, the value of *Pe* is high. In contrast, when the Pe number is less than unity, heat transfer by conduction is the main mechanism of heat dissipation in the pool. The Peclet number is calculated using the average velocity and pool width as the characteristic velocity and length of the weld pool, respectively, and its value is 120 for 312.0 A arc current, 31.0 V voltage, 4.2 mm/s welding speed, and 169.3 mm/s wire feed rate. Because this value is much higher than unity, the liquid metal convection plays a dominant role in dissipating the heat in the weld pool for all of these cases.

The relative importance of the electromagnetic, Marangoni, and buoyancy forces in affecting fluid flow in the weld pool can be determined from the values of appropriate dimensionless numbers. Table II lists the values of all these nondimensional numbers. The ratio of buoyancy force to viscous force is determined by the Grashof number (Gr):[1,4]

$$\mathrm{Gr} = \frac{g\beta L_B^3 \Delta T \rho^2}{\mu^2} \qquad [23]$$

where g is the acceleration due to gravity, β is the thermal expansion coefficient, ΔT is the temperature difference between the peak pool temperature and solidus temperature, ρ is the density of the liquid, μ is the viscosity of

Table II. Values of Various Nondimensional Numbers for 312.0 A Arc Current, 31.0 V Voltage, 4.2 mm/s Welding Speed, and 169.3 mm/s Wire Feed Rate

Nondimensional Variable	Value
Peclet number (Pe)	120
Grash of number (Gr)	11.9
Froude number (Fr)	0.27
Magnetic Reynold's number (Rm)	3.3×10^4
Surface tension Reynold's number (Ma)	2.9×10^4

the liquid, and L_B is a characteristic length for the buoyancy force in the liquid pool and is approximated by one-eighth of the pool radius. For 312.0 A arc current, 31.0 V voltage, 4.2 mm/s welding speed, and 169.3 mm/s wire feed rate, the value of Gr is found to be 11.9. Because the value of the Grashof number is much higher than unity, the viscous force is negligible compared to the buoyancy force during GMA welding.

The ratio of inertia force to gravity force was determined using the Froude number (Fr). It is a dimensionless number that expresses the significance of gravity force in flows with free surface. The Froude number was calculated using the following expression:

$$\mathrm{Fr} \equiv \left[\frac{\text{inertia force}}{\text{gravity force}}\right]^{1/2} = \frac{u}{\sqrt{gH}} \qquad [24]$$

where u is the average liquid velocity in the weld pool and H is the characteristic depth of the liquid pool and is approximated by the value of weld bead throat dimension. If the Froude number is much higher than unity, the inertia effect dominates the flow in the weld pool. If it is much less than unity, the buoyancy or gravity force dominants the liquid metal flow. The value of Fr is 0.27, which suggests that both gravity and inertia force are important during GMA fillet welding.

The magnetic Reynold's number, Rm, defines the ratio of electromagnetic force to viscous force and is expressed as[1,4]

$$\mathrm{Rm} = \frac{\rho\mu_m I^2}{4\pi^2\mu^2} \qquad [25]$$

where μ_m and μ are magnetic permeability and viscosity of the liquid metal, respectively. The value of Rm is 3.3×10^4 for the welding conditions listed in Table II. This value is significantly high, which suggests that the electromagnetic force is very dominant compared to the viscous force for GMA fillet welding.

The surface tension Reynolds number (Ma) is used to describe the ratio of the Marangoni force to viscous force and is calculated as

$$\mathrm{Ma} = \frac{\rho L_R \Delta T \left|\frac{d\gamma}{dT}\right|}{\mu^2} \qquad [26]$$

where L_R is the characteristic length and $d\gamma/dT$ is the surface temperature gradient. The value of Ma is 2.9×10^4, which is of the same order of magnitude as Rm. Table II shows that the value of Gr is very low compared to Rm and Ma, which means that the effect of buoyancy force is very low compared to electromagnetic and Marangoni forces.

The relative importance of the primary driving forces, *i.e.*, surface tension, electromagnetic, and buoyancy forces, can thus be judged by the combination of these dimensionless numbers. For example, the ratio of surface tension force to buoyancy force, $R_{S/B}$, is expressed as

$$R_{S/B} = \frac{\mathrm{Ma}}{\mathrm{Gr}} \qquad [27]$$

while the ratio of electromagnetic force to buoyancy force, $R_{M/B}$, is given by[1,4]

$$R_{M/B} = \frac{\mathrm{Rm}}{\mathrm{Gr}} \qquad [28]$$

For a GMA fillet welding, the values of $R_{S/B}$ and $R_{M/B}$ are found to be 2.4×10^3 and 2.8×10^3, respectively. The values of $R_{S/B}$ and $R_{M/B}$ suggest that the liquid metal flow in the weld pool is driven primarily by the Marangoni and electromagnetic forces and, to a much lesser extent, by the buoyancy force. Furthermore, the value of $R_{M/B}$ was more than double during GMA fillet welding compared to GTAW.[25] This suggests that the electromagnetic force plays a more important role during GMA fillet welding, mainly because the arc current used in this process is much higher than that in GTAW.

C. *Effect of Workpiece Orientations on Temperature Distribution, Velocity Fields, and Free Surface Profile*

The calculated temperature and velocity fields during welding of symmetrical V shape along the horizontal, L-shaped geometry along the horizontal, downhill, and uphill welding of V-shaped configuration are shown in Figures 3, 4, 5, and 6, respectively. These figures show the variation of surface profile at different transverse cross sections perpendicular to the welding directions. The region directly under the arc for symmetrical V-shaped joint is shown in Figure 3(a). This figure also shows the depression of the free surface due to the arc force. The temperature profiles in Figure 3(a) clearly show the finger penetration characteristic of GMA welding. The weld pool surface is severely depressed under the effect of the arc pressure, and the liquid metal flows downward in the middle of the pool driven by the electromagnetic force. As the monitoring location moves away from the arc, the weld pool surface shows considerably less depression, as would be expected from the reduction in arc pressure. Furthermore, the

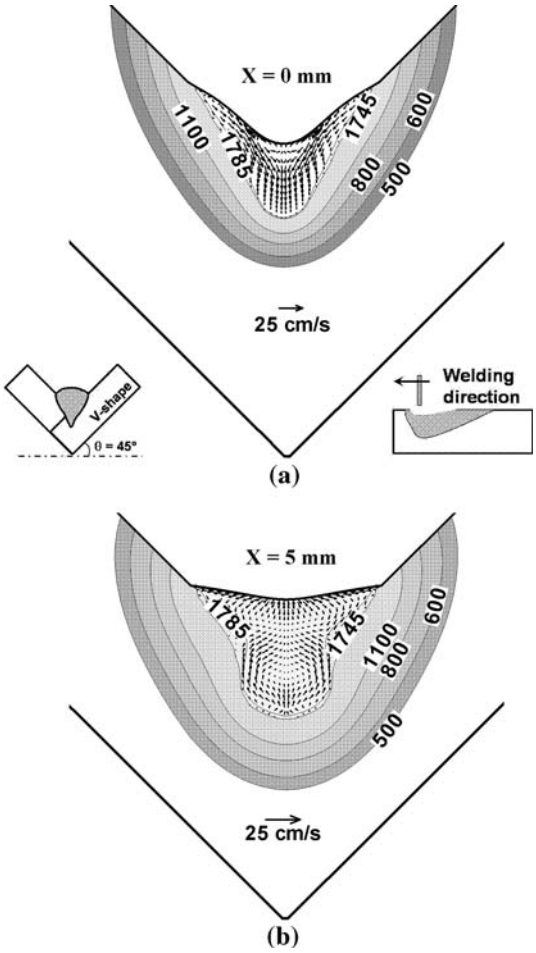

Fig. 3—Calculated temperature field and velocity fields during horizontal welding of symmetrical V-shaped joint, as shown in the inset. The temperatures are given in Kelvin. The temperature and velocity fields at different cross-sectional planes perpendicular to the welding direction are shown in (a) and (b). These figures represent the following regions: (*a*) directly under the arc and (*b*) 5 mm rear of the arc location.

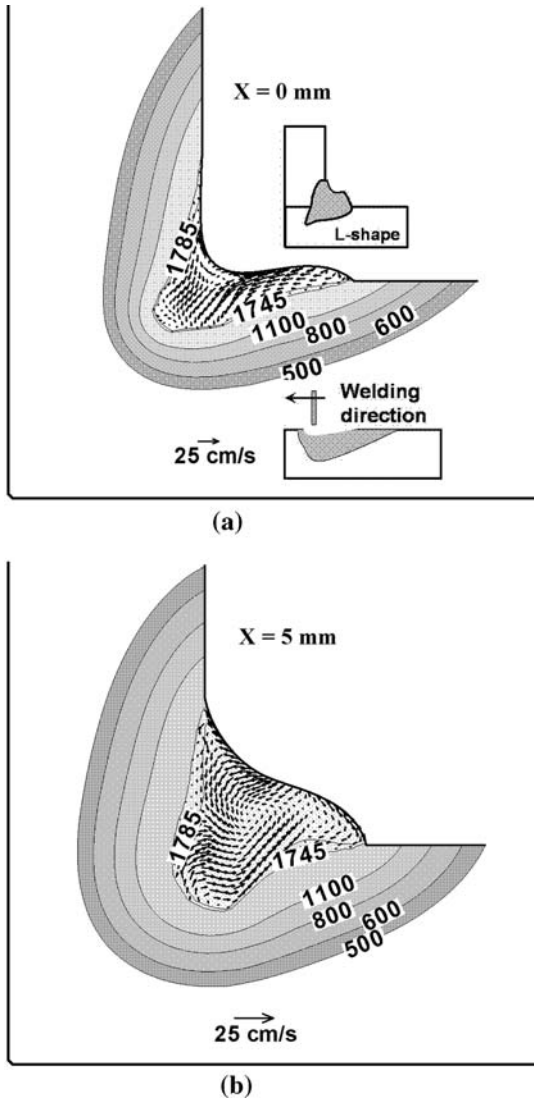

Fig. 4—Calculated temperature field and velocity fields during horizontal welding of L-shaped joint. The temperatures are given in Kelvin. The temperature and velocity fields at different cross-sectional planes perpendicular to the welding direction are shown in (a) and (b). These figures represent the following regions: (*a*) directly under the arc and (*b*) 5 mm rear of the arc location.

accumulation of the liquid metal in the rear of the weld pool is clearly visible in Figure 3(b).

Figures 4 through 6 show a similar finger penetration characteristic of the GMA welding during horizontal welding of L-shaped joint and downhill and uphill welding of V-shaped joints. However, due to the effect of inclination of the workpiece, the buoyancy and inertia force affect the temperature distribution and the velocity field in the workpiece, as shown in Figures 4 through 6. Downhill welding affects the weld contour and penetration, as shown in Figure 5. The weld puddle tends to flow toward the electrode and preheats the base metal, particularly at the surface. As the angle of declination increases, the middle surface of the weld is depressed, penetration decreases, and the width of weld increases. Uphill welding affects the fusion zone and the weld surface, as shown in Figure 6. With an increase in the angle of inclination, the penetration increases while the width of the weld pool decreases because the liquid metal tends to flow opposite to the welding direction due to gravity force.

Figures 7(a) through (d) show the calculated solidified weld bead geometry during welding of symmetrical V shape along the horizontal, L-shaped geometry along the horizontal, downhill, and uphill welding of V-shaped configuration. These figures are obtained by projecting the transverse planes on each other. These figures show that the solidified region behind the arc is elevated owing to the filler metal addition. This accumulated metal forms the weld reinforcement after solidification. Furthermore, the free surface profile differs quite remarkably depending on the workpiece orientations and welding positions in these cases. This difference in weld bead geometry may affect the strength and integrity of the welded joint.[22]

Table III lists the calculated weld bead dimensions, Froude number (Fr), and magnitude of maximum

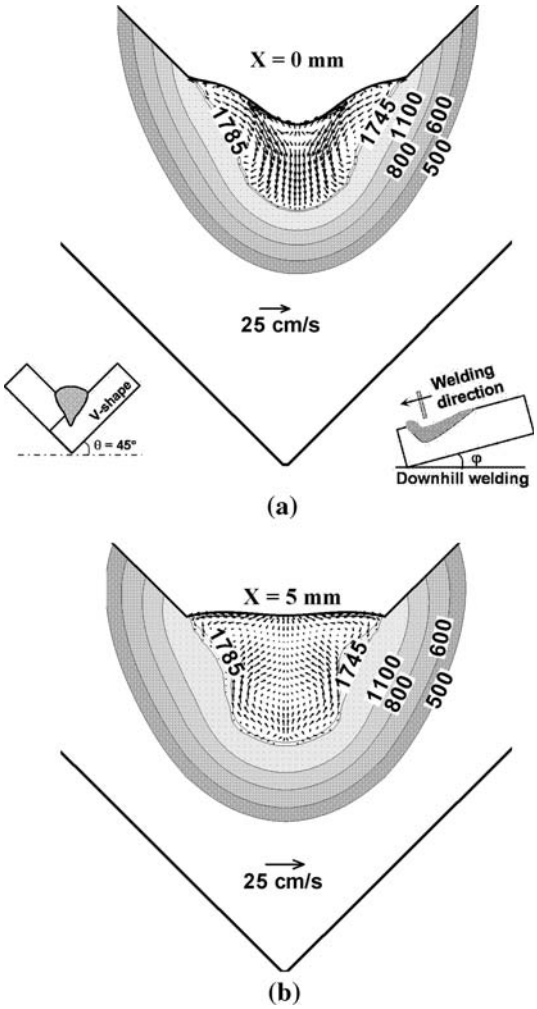

Fig. 5—Calculated temperature field and velocity fields during downhill welding of V-shaped joint. The workpiece is lifted from behind the electrode at an angle of 10 deg. The temperature and velocity fields at different cross-sectional planes perpendicular to the welding direction are shown in (a) and (b). These figures represent the following regions: (*a*) directly under the arc and (*b*) 5 mm rear of the arc location.

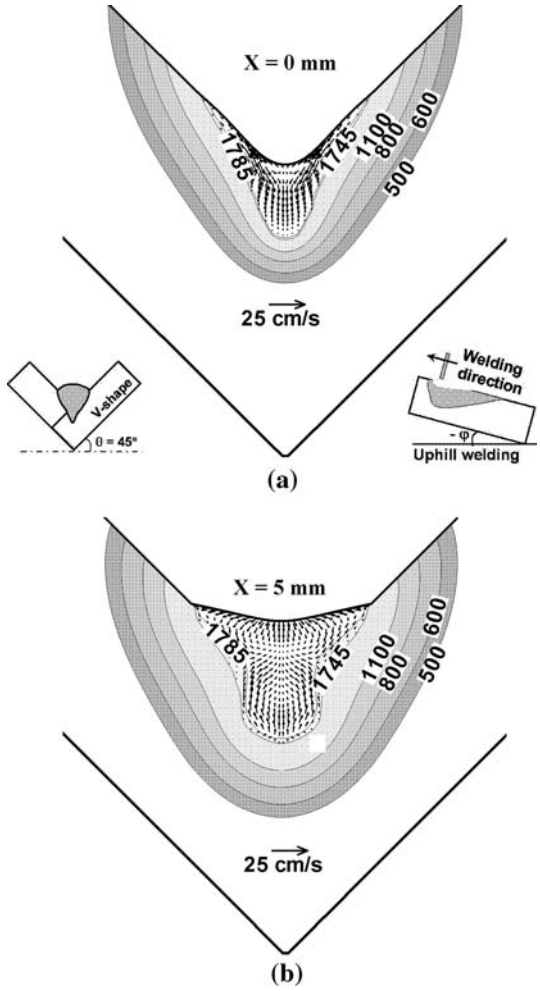

Fig. 6—Calculated temperature field and velocity fields during uphill welding of V-shaped joint. The workpiece is lifted from ahead of the electrode at an angle of 10 deg. The temperature and velocity fields at different cross-sectional planes perpendicular to the welding direction are shown in (a) and (b). These figures represent the following regions: (*a*) directly under the arc and (*b*) 5 mm rear of the arc location.

velocities in all four cases. The high value of Fr during downhill welding signifies the dominance of the inertia force over the gravity force. In the case of L-shaped joint, the Fr is low, which means that the gravity plays an important role in this situation, which is also evident from the free surface obtained in Figure 7(b). Table III also shows that the horizontal and vertical leg-length dimensions are higher during downhill welding compared to other welding positions. This is due to downward flow of the liquid under the gravity force, which tries to force the liquid in an outward direction toward the plate edges. This effect can be justified through Figure 7(c), where the free surface profile is depressed in the center. Furthermore, during uphill welding, the throat dimension increases compared to horizontal or downhill welding, because the molten metal starts solidifying in the central region, as can be seen in Figure 7(d). Similar trends were observed by Kang *et al.*[38] during gas-tungsten-arc butt welding of nickel. Their experimental data showed that uphill welding at 90 deg produces 21 pct deeper penetration compared to perpendicular downhill welding at low welding speeds. During downhill welding, the extra mass is accumulated ahead of the arc, which leads to a shallow weld pool. They also observed about 5 to 8 pct increase in the width of the weld pool during the downhill position at 3 mm/s welding velocity. They attributed this change in weld dimensions to free surface deformation, which they measured using laser profilometry. These experimental results in the literature[38] qualitatively support the results obtained in the present work for the more complex GMA fillet welding system.

The calculated temperature and velocity fields and surface profile at the central vertical longitudinal sections parallel to the welding direction are shown in Figure 8, where the weld pool boundary is represented

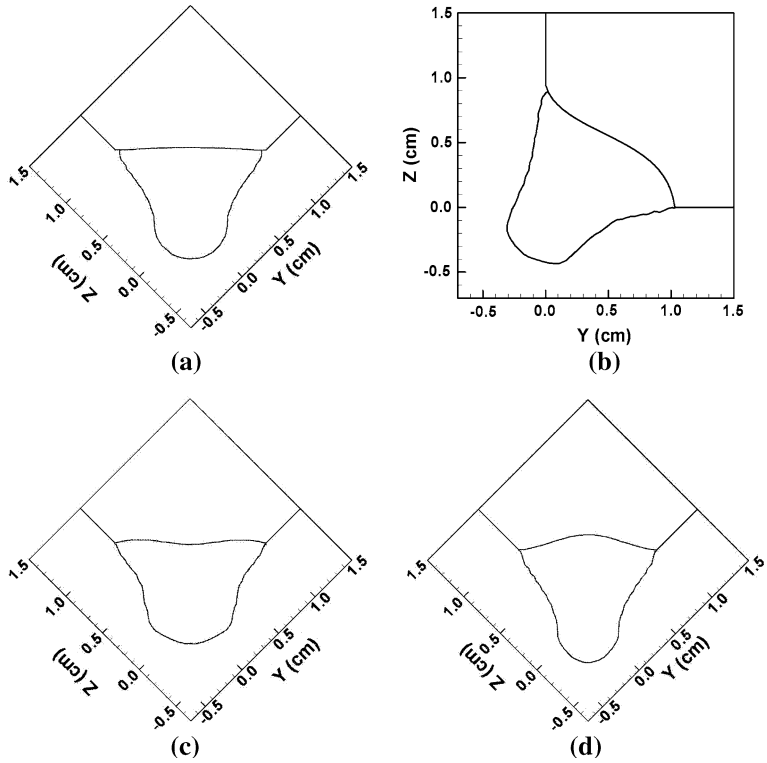

Fig. 7—The solidified reinforced weld bead geometry during (*a*) horizontal welding of V-shaped fillet joint, (*b*) horizontal welding of L-shaped fillet joint, (*c*) downhill welding of V-shaped fillet joint at an angle of 10 deg, and (*d*) uphill welding of V-shaped fillet joint at an angle of 10 deg. The calculated weld bead geometries in these figures are obtained by projecting the transverse planes over each other.

Table III. Effect of Different Orientations of Workpiece on the Liquid Velocity, Weld Pool Dimensions, and Froude Number (Fr); Symbols u_{max}, v_{max}, and W_{max} Represent the Maximum Velocity (Magnitude) in *x*, *y*, and *z* Directions, Respectively

Join Configuration and welding position	u_{max} (mm/s)	v_{max} (mm/s)	w_{max} (mm/s)	Vertical Leg Length (mm)	Horizontal Leg Length (mm)	Throat (mm)	Fr
V-shaped geometry and horizontal welding	176.3	177.9	111.4	9.8	9.8	10.8	0.27
L-shaped geometry and horizontal welding	151.0	186.9	133.0	8.8	10.3	10.7	0.24
V-shaped geometry and 10 deg uphill welding	185.2	157.8	116.3	9.5	9.5	11.7	0.28
V-shaped geometry and 10 deg downhill welding	221.3	212.8	109.5	10.3	10.3	9.6	0.36

by the 1745 K solidus isotherm. As shown in all of these figures, the liquid metal motion is quite complicated due to the combined effects of the driving forces. In the middle of the weld pool, the liquid metal is driven downward by the electromagnetic force, and a major anticlockwise circulation loop is formed along the central longitudinal plane, *i.e.*, $Y = 0$ plane shown in Figure 8. The region directly under the heat source is severely depressed under the effect of arc pressure. As a result of the filler metal addition, the solidified weld metal forms pronounced weld reinforcement. Figure 8(c) shows the molten metal ahead of the arc (which is located at $X = 2.5$ cm) due to downward flow of liquid metal under the effect of inertia force. This downward flow tries to deform the weld pool surface from the center. In the case of uphill welding, there is no hump of liquid metal ahead of the arc because the gravity force tries to carry all the molten metal toward the rear end (Figure 8(d)). These figures also show that, away from the heat source, the weld pool surface shows considerably less depression, as would be expected from the reduction in arc pressure. Also, the peak temperatures are higher at locations close to the weld center and decrease away from the heat source.

Figures 9(a) through (d) show the comparison between the calculated weld bead shape for GMA fillet welding of V-shape, L-shaped joints, downhill welding, and uphill welding. As shown in these figures, the calculated weld bead geometries agree reasonably well with the corresponding experimental results. In particular, the shape of the weld reinforcement and the finger penetration could be satisfactorily predicted by the model. Some discrepancy between the experimental surface profile and the computed results is due to thermal stress-induced distortion, as can be evidenced from the gap between the two

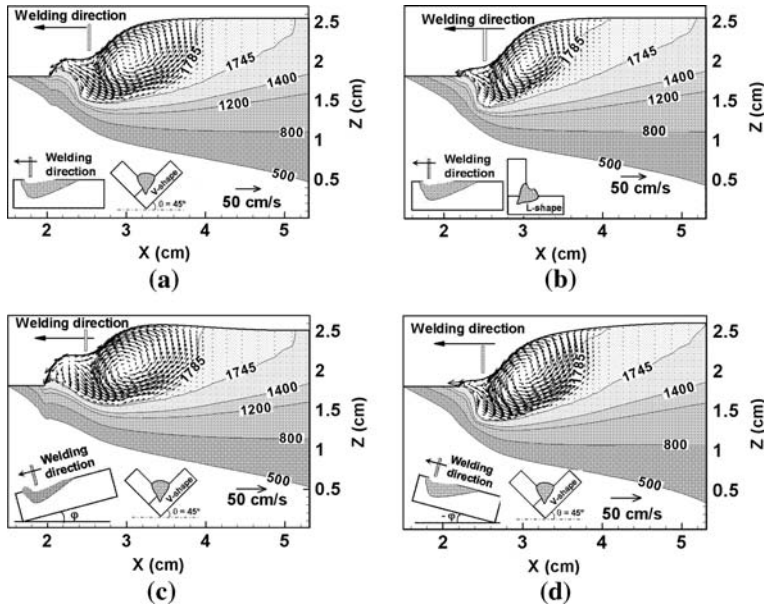

Fig. 8—Calculated temperature and velocity vectors (shown by arrows) along central vertical longitudinal plane, *i.e.*, plane AB as shown in the inset. (*a*) Horizontal welding of V-shaped joint, (*b*) horizontal welding of L-shaped joint, (*c*) downhill welding of V-shaped joint at an angle of 10 deg, and (*d*) uphill welding of V-shaped joint at an angle of 10 deg. All the temperatures are given in Kelvin. The weld pool boundary is represented by the 1745 K isothermal line. Electrode is located at $X = 2.5$ cm.

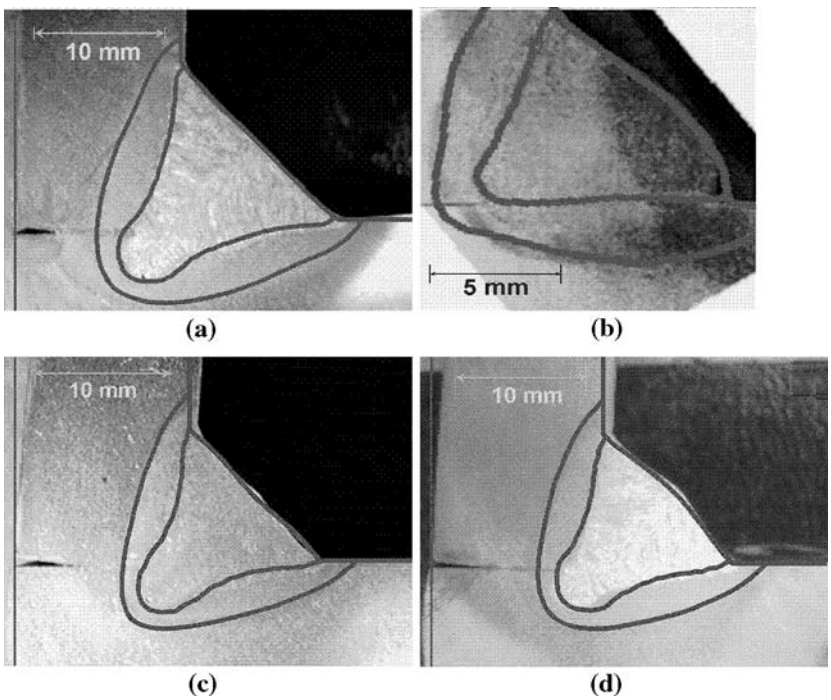

Fig. 9—Comparison between the calculated and experimental weld geometry during GMA welding of (*a*) V-shaped symmetric fillet joint using $I = 362$ A, $V = 33$ V, $U = 4.2$ mm/s, and $w_f = 211.7$ mm/s; (*b*) L-shaped symmetric fillet joint using $I = 250$ A, $V = 29$ V, $U = 7.0$ mm/s, and $w_f = 150.0$ mm/s; (*c*) downhill welding at lift angle = 6 deg using $I = 362$ A, $V = 33$ V, $U = 6.4$ mm/s, and $w_f = 211.7$ mm/s; and (*d*) uphill welding at lift angle = −4 deg using $I = 322.6$ A, $V = 32$ V, $U = 5.3$ mm/s, and $w_f = 190.5$ mm/s. The experimental micrograph in (b) is taken from Ref. 21. The inner isotherm (blue line) in all these figures represents the calculated weld pool boundary based on solidus temperature of 1745 K, while outer isotherm (blue line) represents the 1073 K temperature.

plates. Slight uncertainty in the values of various input parameters such as arc efficiency, arc radius, and droplet frequency may also affect the computed weld geometry. On the whole, the geometric features of the fillet weld could be satisfactorily predicted by using the numerical heat transfer and fluid flow model.

D. *Effect of Arc Current and Orientation Angles on the Weld Pool Geometry*

Because the weld bead geometric characteristics affect the mechanical properties of the fillet weld, the effect of arc current and workpiece tilt angle on the weld geometry is studied. Figure 10 shows three important geometrical parameters of the weld bead, *i.e.*, horizontal leg length, vertical leg length, and throat, as a function of the welding current and the workpiece tilt angle. As shown in this figure, the computed results show that the geometrical parameters increase with the arc current as expected. For a fillet weld, the arc energy input is primarily responsible for the formation of the top part of the weld bead, whereas the volumetric heat source is largely responsible for the formation of the finger penetration. An increase in arc current increases the heat supplied to the workpiece, downward electromagnetic force, arc pressure, and droplet frequency. An increase in all of these factors increases the weld bead dimensions.

With an increase in tilt angle, the horizontal length and throat decrease while the vertical leg length increases (Figures 10(a) through (c)). This is due to the inertia effect, which tries to pull down the liquid metal in the downward direction. An increase in tile angle increases the difference between horizontal and vertical leg lengths, which may affect the final strength of the weld bead. Figure 10(c) shows that the computed nondimensional throat does not vary significantly with either arc current or tilt angle for a given wire feed rate and welding speed. This behavior is expected because the dimensions of the throat depend largely on the rate of mass addition.

E. *Weld Thermal Cycles and Cooling Rates*

The temperature field obtained from the heat-transfer and fluid-flow calculation is at quasi-steady state, because the coordinate system is attached to the moving heat source. Therefore, the thermal cycles are calculated by converting the x distance into time using the welding speed. Figure 11 shows the thermal cycles at four different monitoring locations within the fusion zone during welding of the L-shaped fillet joint. As shown in this figure, the heating rates are much higher than the cooling rates. This is due to the following two reasons. First, the isotherms in front of the heat source are compressed, whereas those behind it are largely elongated due to the high welding speed. Second, the existence of the volumetric heat source also contributes to the high heating rates. As expected, the peak temperatures are higher at locations close to the weld center and decrease as the monitoring location moves farther away. Furthermore, the cooling rate at location 2 is much faster compared to other locations because it is closer to the workpiece sides, which are nearly at room temperature. Figure 11 also shows that the thermal cycles are different for locations 3 and 4 due to unsymmetric weld bead geometry, which affects the temperature distribution inside the workpiece. This difference in peak temperature and thermal cycles at any particular location affects the microstructure and the residual stress inside the workpiece.

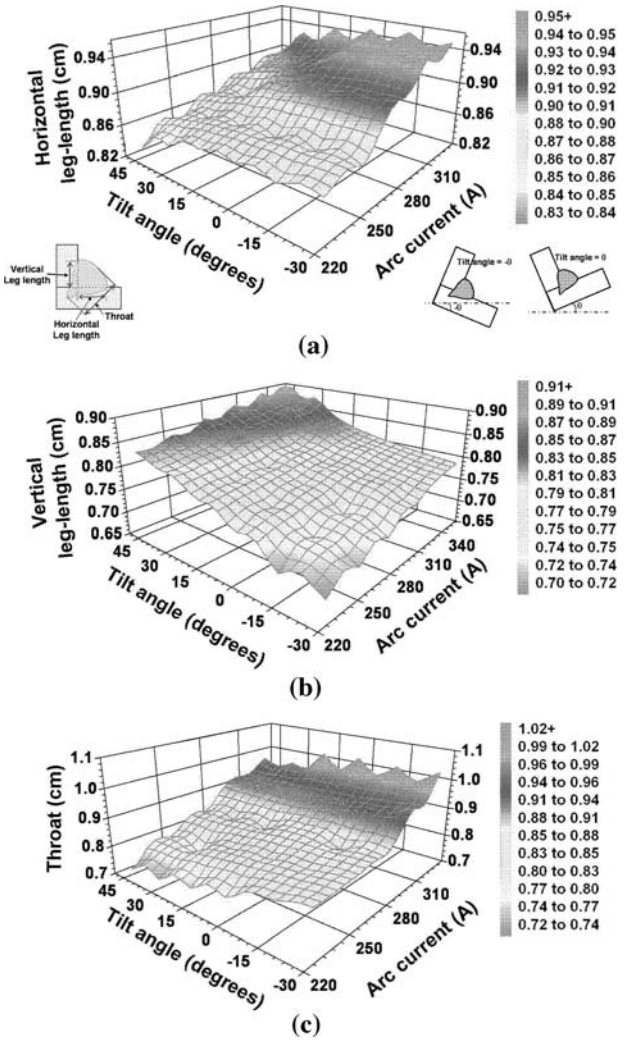

Fig. 10—Effect of arc current and the workpiece tilt angle on (*a*) horizontal leg length, (*b*) vertical leg length, and (*c*) throat of the weld bead. Tilt angle = 0 deg refers to V-shaped joint and 45 deg refers to L-shaped joint.

During welding of steel plates, the average cooling rate, $\dot{T}_{8/5}$, from 1073 to 773 K (800 °C to 500 °C) is of importance, because it affects the final microstructure of the weld metal for most of the steels.[1,2,39] Figures 12(a) and (b) show the calculated average cooling rates at different monitoring locations for different orientations of workpiece plates (*i.e.*, V and L configurations) and during uphill and downhill welding, respectively. As shown in these figures, the calculated average cooling rate decreases as the heat input per unit length (defined as the total power input/welding speed) increases. The effect of heat input per unit length on $\dot{T}_{8/5}$ can be explained as follows. The average cooling rate $\dot{T}_{8/5}$ is calculated as

$$\dot{T}_{8/5} = \frac{T_{800} - T_{500}}{t_{8/5}} = \frac{300 \times U_w}{\Delta d_{8/5}} \qquad [29]$$

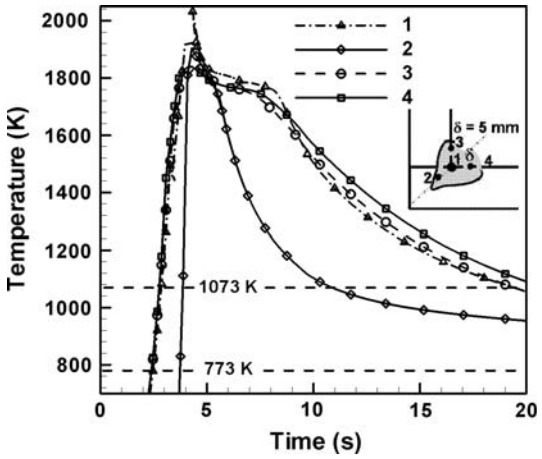

Fig. 11—Calculated thermal cycles in the fillet weld at four different locations during horizontal welding of L-shaped joint. Symbol δ represents the distance from the joint root to the monitoring locations, as shown in the inset.

where $t_{8/5}$ is the cooling time from 1073 to 773 K, U_w is the welding speed, and $\Delta d_{8/5}$ is the distance between two points where a line parallel to the x direction intercepts the 1073 and 773 K isothermal contours. With an increase in welding speed, both the 1073 and 773 K isothermals expand outward. However, the distance $\Delta d_{8/5}$ does not change significantly. As a result, the cooling rate increases. Because an increase in U_w is accompanied by a reduction in the heat input per unit length, a reduction in heat input is thus accompanied by an increase in the cooling rate, as observed in Figures 12(a) and (b). On the other hand, when input power is increased while maintaining the constant welding speed, the isotherms are expanded and $\Delta d_{8/5}$ increases. Hence, the cooling rate decreases with an increase in the input power. Because both a decrease in the welding speed and an increase in the power input result in a reduction in the cooling rate, the higher the heat input per unit length, the lower the cooling rate $\dot{T}_{8/5}$.

Figures 12(a) and (b) also indicate that the average cooling rates away from the weld central line are higher than those at the central axis on the weld bead top surface. This is because the temperature near the workpiece edges is much lower compared to the center of the weld bead, which helps in faster cooling. Figure 12(a) also shows that due to unsymmetrical weld bead formation, the cooling rates are different at the two ends of the weld bead. Furthermore, the cooling rates are higher during downhill welding compared to uphill welding. This is due to wider weld bead formation during downhill welding (Figure 12(b)), which brings the end of the fusion zone much nearer to the edges of the workpiece. The cooling rate increases as we move away from the center of the weld bead. A 10 to 25 pct increase in cooling rate can be observed between locations I and II in Figures 10(a) and (b). Furthermore, this difference in cooling rate increases with an increase in heat input per unit length. In the literature, a nomograph[39] is commonly used to estimate the average cooling rate $\dot{T}_{8/5}$ for various welding conditions.

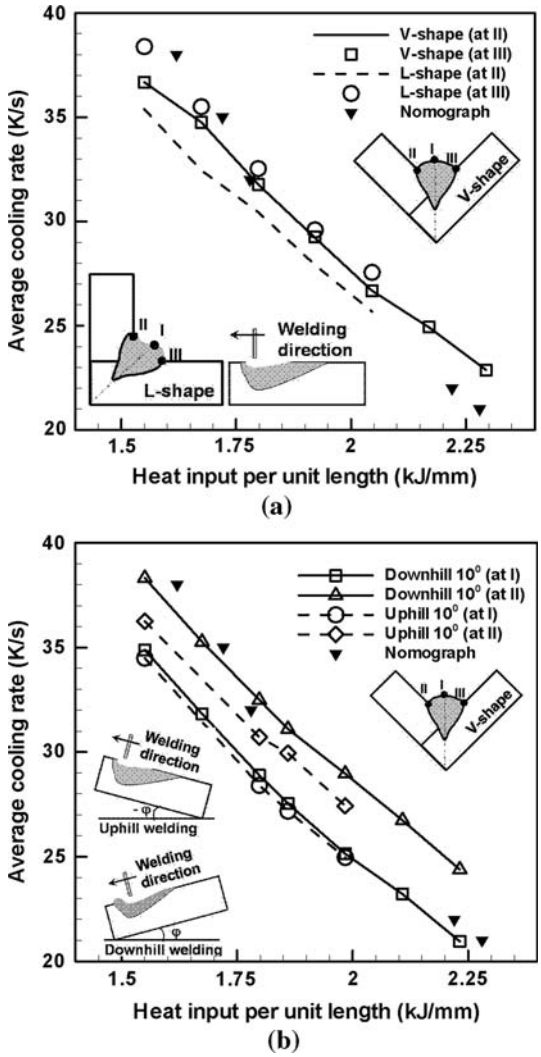

Fig. 12—Calculated average cooling rate $\dot{T}_{8/5}$ at different monitoring locations in the fillet weld for (*a*) different orientations of workpiece and (*b*) during downhill and uphill welding of V-shaped geometry. The solid triangles represent the cooling rate estimated using the nomograph available in the literature.[39].

As shown in Figures 12(a) and (b), the calculated cooling rates at the fusion boundary agree reasonably well with those estimated using the nomograph.[39] This good agreement indicates the validity of the heat-transfer and fluid-flow calculation during GMA fillet welding. Furthermore, the heat-transfer and fluid-flow model is capable of providing much more information on cooling rates than the nomograph, such as the spatial variation of the cooling rate for different orientations of workpiece.

Figures 13(a) and (b) show the effect on welding positions and orientation, *i.e.*, lift and tilt angles, respectively, on $\dot{T}_{8/5}$. The value of $\dot{T}_{8/5}$ increases with the increase in lift angle, which means that the cooling rates are much higher during downhill welding compared to uphill or flat welding positions. The cooling rates during uphill welding are lowest among the three inclined positions, *i.e.*, uphill, flat, and downhill welding. This is due to the low molten metal toward the rear of

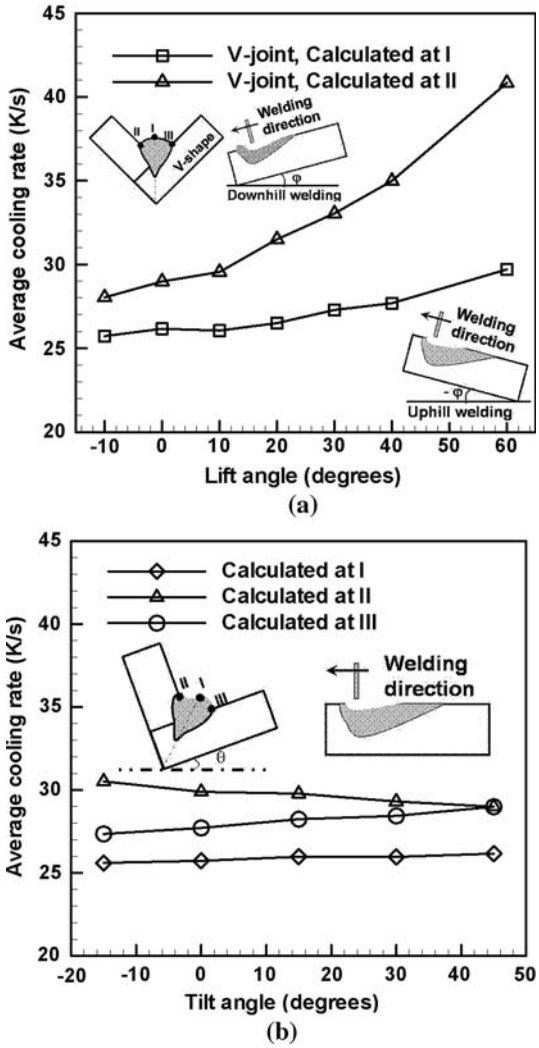

Fig. 13—Effect of the (*a*) lift angle and (*b*) tilt angle on the avergae cooling rates ($\dot{T}_{8/5}$) from 1073 to 773 K at different monitoring locations during GMA fillet welding.

the welding torch under the influence of gravity during uphill welding. The heat carried by the molten metal slows the cooling process behind the electrode during uphill welding. In the case of downhill welding, the flow of molten metal in the welding direction transports heat from the rear to the front of the weld pool and increases the cooling rate. Figure 13(a) also shows that the cooling rates at location II are much higher than those at location I because location II is much nearer to the edges of the workpiece. With an increase in tilt angle, the cooling rate increases slightly. This may be due to more uniform and symmetrical bead formation, which favors uniform distribution of the heat. However, there is not much effect of the tilt angle on the cooling rate, as shown in Figure 13(b). The results obtained in this work helps in better quantitative understanding of the effect of fillet joint geometry (*i.e.*, tilt angle) and welding positions (*i.e.*, lift angle) on weld bead geometry, free surface, thermal cycles, and cooling rates inside the workpiece.

IV. SUMMARY AND CONCLUSIONS

A numerical heat-transfer and fluid-flow model of GMA fillet welding is developed to understand the effects of fillet joint orientations on free surface profile, temperature distribution, velocity field, weld pool shape and size, and nature of the solidified weld pool reinforcement surface. The following conclusions can be drawn from the results.

1. The liquid metal convection plays a dominant role in dissipating the heat in the weld pool for all orientations of the workpiece, *i.e.*, V and L joint configurations and horizontal, downhill, and uphill welding positions. The velocities in the weld pool are found to be fairly high, which affects the weld pool shape and mixing of the solutes and gases in the weld pool.
2. The workpiece orientations and welding configuration significantly affect the free surface profile. During L-shaped joints, the free surface profile becomes asymmetrical due to gravity, which affects the strength of the weld bead.
3. The horizontal leg length and vertical leg length are found to increase during downhill welding, while these dimensions decrease during uphill welding. The throat dimension has the opposite effect of welding position, and it increases during uphill welding.
4. The geometrical parameters such as throat, horizontal leg length, and vertical leg length increase with the increase in arc current. It is also observed that, with the increase in tilt angle from −30 to 45 deg, the horizontal length and throat decrease while the vertical leg length increases.
5. The computed results show that the thermal cycles at various locations inside the workpiece vary with the change in workpiece orientations or welding positions. It is found that with an increase in the lift angle, the average cooling rate between 1073 and 773 K ($\dot{T}_{8/5}$) increases for similar welding conditions. Therefore, average cooling rates for downhill welding are higher than uphill or flat welding positions. Both the calculated results and the available experimental data indicate that $\dot{T}_{8/5}$ decreases with the increase in heat input per unit length. The calculated results are in good agreement with the independent experimental data available in the literature.
6. The numerically computed fusion zone geometry, finger penetration characteristic of the GMA welds, and solidified surface profile of the weld reinforcement are in fair agreement with the experimental result.

REFERENCES

1. W. Zhang, C.H. Kim, and T. DebRoy: *J. Appl. Phys.*, 2004, vol. 95, pp. 5210–19.
2. W. Zhang, C.H. Kim, and T. DebRoy: *J. Appl. Phys.*, 2004, vol. 95, pp. 5220–29.

3. A. Kumar and T. DebRoy: *Metall. Mater. Trans. A*, 2005, vol. 36 (10), pp. 2725–35.
4. W. Zhang, G.G. Roy, J.W. Elmer, and T. DebRoy: *J. Appl. Phys.*, 2003, vol. 93, pp. 3022–33.
5. M.C. Tsai and S. Kou: *Weld. J.*, 1990, vol. 69, pp. 241s–46s.
6. K. Hong, D.C. Weckmann, A.B. Strong, and W. Zheng: *Sci. Technol. Weld. Join.*, 2002, vol. 7, pp. 125–36.
7. K. Mundra, T. DebRoy, and K. Kelkar: *Numer. Heat Transfer A*, 1996, vol. 29, pp. 115–29.
8. Z. Yang, J.W. Elmer, J. Wong, and T. DebRoy: *Weld. J.*, 2000, vol. 79, pp. 97s–112s.
9. Z. Yang, S. Sista, J.W. Elmer, and T. DebRoy: *Acta Mater.*, 2000, vol. 48, pp. 4813–25.
10. T. Hong, W. Pitscheneder, and T. DebRoy: *Sci. Technol. Weld. Join.*, 1998, vol. 3, pp. 33–41.
11. R.T.C. Choo and J. Szekely: *Weld. J.*, 1994, vol. 73, pp. 25–31.
12. J.F. Lancaster: *The Physics of Welding*, 2nd ed., Pergamon, Oxford, United Kingdom, 1986, pp. 49–94.
13. C.S. Wu and L. Dorn: *Comput. Mater. Sci.*, 1994, vol. 2, pp. 341–50.
14. J.W. Kim and S.J. Na: *Weld. J.*, 1995, vol. 74, pp. 141–52.
15. Z.N. Cao and P. Dong: *J. Eng. Mater. Technol.*, 1998, vol. 120, pp. 313–20.
16. H.G. Fan and R. Kovacevic: *J. Phys. D: Appl. Phys.*, 1998, vol. 31, pp. 2929–41.
17. Y. Wang and H.L. Tsai: *Metall. Mater. Trans. B*, 2001, vol. 32, pp. 501–15.
18. C.H. Kim, W. Zhang, and T. DebRoy: *J. Appl. Phys.*, 2003, vol. 94, pp. 2667–79.
19. S. Kumar and S.C. Bhaduri: *Metall. Mater. Trans. B*, 1994, vol. 25, pp. 435–41.
20. S.-K. Jeong and H.-S. Cho: *Welding J.*, 1997, vol. 76 (6), pp. 223–32.
21. S.-H. Cho and J.-W. Kim: *Sci. Technol. Weld. Join.*, 2001, vol. 6 (4), pp. 220–24.
22. W.A. Bowditch and K.E. Bowditch: *Welding Technology Fundamentals*, 2nd ed., The Goodheart–Willcox Company, Tinley Park, IL, 1997, pp. 64–82.
23. V.R. Voller and C. Prakash: *Int. J. Heat Mass Transfer*, 1987, vol. 30, pp. 1709–19.
24. A.D. Brent, V.R. Voller, and K.J. Reid: *Numer. Heat Transfer A*, 1988, vol. 13, pp. 297–318.
25. A. Kumar and T. DebRoy: *J. Appl. Phys.*, 2003, vol. 94, pp. 1267–77.
26. S. Kou and D.K. Sun: *Metall. Trans. A*, 1985, vol. 16A, pp. 203–12.
27. S. Rhee and E. Kannatey-Asibu Jr.: *Weld. J.*, 1992, vol. 71, pp. 381–86.
28. L.A. Jones, T.W. Eagar, and J.H. Lang: *J. Phys. D: Appl. Phys.*, 1998, vol. 31, pp. 107–23.
29. P. Sahoo, T. DebRoy, and M.J. McNallan: *Metall. Trans. B*, 1988, vol. 19B, pp. 483–91.
30. W. Pitscheneder, T. DebRoy, K. Mundra, and R. Ebner: *Welding J.*, 1996, vol. 75, pp. 71s–80s.
31. M.L. Lin and T.W. Eagar: *Metall. Trans. B*, 1986, vol. 17B, pp. 601–07.
32. Y.S. Kim and T.W. Eagar: *Weld. J.*, 1991, vol. 70, pp. 20–31.
33. W.H. Press, B.P. Flannery, S.A. Teukolsky, and W.T. Vetterling: *Numerical Recipes in FORTRAN*, 2nd ed., Cambridge University Press, Cambridge, United Kingdom, 1992, pp. 855–64.
34. K.A. Hoffmann and S.T. Chiang: *Computational Fluid Dynamics for Engineering*, Vol. II, Engineering Education System, Wichita, KS, 1993, pp. 124–87.
35. J.F. Thompson, Z.U.A. Warsi, and C.W. Mastin: *Numerical Grid Generation: Foundations and Applications*, , Elsevier Science, New York, NY, 1985, pp. 45–94.
36. S.V. Patankar: *Numerical Heat Transfer and Fluid Flow*, 2nd ed., Hemisphere Publishing, New York, NY, 1982, pp. 41–71.
37. E.A. Brandes and G.B. Brook: *Smithells Metals Reference Book*, 7th ed., Butterworth-Heinemann, Oxford, United Kingdom, 1992, pp. 1430–43.
38. N. Kang, T.A. Mahank, A.K. Kulkarni, and J. Singh: *J. Mater. Manuf. Proc.*, 2003, vol. 18 (2), pp. 169–80.
39. K. Masubuchi: *Analysis of Welded Structures*, 1st ed., Pergamon, Oxford, United Kingdom, 1980, pp. 74–98.